Ship Target Imaging in Airborne SAR System Based on Automatic Image Segmentation and ISAR Technique

Rui Cao, Yong Wang ![ORCID], *Senior Member, IEEE*, Bin Zhao, and Xiaofei Lu ![ORCID]

Abstract—The airborne synthetic aperture radar (SAR) image of ship target will be blurred for the complex motion of the target, which will influence the performance of feature extraction and target classification. In this article, a refocusing method of ship target in airborne SAR image though the inverse synthetic aperture radar (ISAR) technique is presented. The novel contributions of this article can be summarized as follows: 1) the residual phase of processed signal is analyzed in detail to illustrate the necessity of adopting ISAR technique; 2) a valid, labor-saving, and automatic image segmentation approach via clustering algorithm is put forward for automatic data extraction and inverse mapping. The clustering algorithm we choose is the agglomerative hierarchical cluster algorithm, which does not require the number of categories in advance; 3) the refocused individual ISAR image of individual ship target is yielded though the range-instantaneous Doppler algorithm. Finally, the simulated and real measured data are processed, and imaging results verify the effectiveness of the novel algorithm presented in this article.

Index Terms—Automatic image segmentation, clustering algorithm, hierarchical cluster algorithm (HCA), inverse synthetic aperture radar (ISAR) refocusing, ship target, synthetic aperture radar (SAR).

I. INTRODUCTION

SYNTHETIC aperture radar (SAR) has achieved a stupendous development in the numerous domains, such as the terrain mapping, marine observation, and disaster forecasting [1]–[3]. As is well-known, in the SAR imaging, radar is carried by the satellite or aircraft to image the stationary scene, generally. However, some specific scenes contain moving targets, such as ships on the sea surface, which will cause blurring of the SAR image [4]–[6]. The reason is that the imaging geometry contains both radar and target motions during the whole imaging process. However, the SAR processing algorithm only cares about the radar motion [7]–[10]. Therefore, how to achieve high-quality

images of moving ship targets in SAR imaging has brought about many attentions.

For this issue, there are three kinds of approaches, which are as follows

1) Considering the whole process as SAR imaging, the target motion is compensated in the SAR processing.
2) Considering the whole process as inverse synthetic aperture radar (ISAR) imaging, the movement of radar is compensated via the ISAR imaging algorithm.
3) SAR and ISAR algorithms are combined to solve this problem, that is hybrid SAR/ISAR imaging. The SAR image of the entire scene is attained first, then the equivalent data is obtained via inverse mapping, and finally the ISAR algorithm is applied for refocusing each moving target in the scene, respectively.

Pelich *et al.* [11], Jao [12], Zhou *et al.* [13], Yang, and Zhang [14]; and Gu *et al.* [15] adopted the first kind of approaches, which can generate the focused images of moving targets by estimating targets' motion parameters. Nevertheless, the improvement of image quality depends on the accuracy of target motion modeling [4]. In the second scenario, echo data of the entire scene is processed by the ISAR technique, which implies that the movements of SAR platform and targets are compensated simultaneously. However, motions of SAR and each target are different and the individual target's echo is unable to be separated from the echo of scene. Therefore, this kind of methods are difficult to compensate the movements of all targets. Moreover, it does not take full advantage of the prior motion information about SAR platform. In [4]–[10], by jointly adopting the SAR and ISAR imaging algorithms, the motions of targets and SAR platform are processed respectively. The hybrid SAR/ISAR imaging algorithms obtain the image of entire scene with SAR processor first. Then, images containing a single target are acquired by image segmentation. Afterward, the received-like data of individual ship target can be attained via inverse mapping. Finally, refocused images of each moving target are achieved with ISAR processing. Owing to employing prior information provided by the SAR platform appropriately, no necessarily knowing motion parameters of moving targets and no restricting the motion modeling, the hybrid SAR/ISAR imaging algorithms are popular among experts and scholars. Hence, the hybrid SAR/ISAR imaging methods are widely used in the practical applications.

However, there are still several drawbacks to the hybrid SAR/ISAR imaging algorithm, especially manually implementing the image segmentation that limits its application in the practical imaging scenarios. In this article, we present a novel SAR/ISAR imaging approach based on the automatic image segmentation by which focused images of ship targets can be attained. The main procedures of the proposed approach are concluded as follows.

1) First, a SAR image of the whole scene is obtained via appropriate SAR processing approach.
2) Then, the scatterers represented by the SAR image are clustered via the appropriate clustering algorithm.
3) The SAR images of each ship target are acquired by a 2-D filter which is designed based on the clustering results.
4) Finally, the equivalent data acquired by the inverse mapping is processed by the ISAR technique and the refocused ISAR images of each target are achieved. Importantly, the whole hybrid SAR/ISAR imaging process is automatic, from image segmentation to inverse mapping and to ISAR refocusing.

In this article, we select the agglomerative single-linkage hierarchical clustering algorithm (HCA) to accomplish the automatic image segmentation, which is a "bottom-up" approach. At first, each object is regarded as an individual cluster in the procedure of HCA. Then, in each iteration, two clusters owning minimum distance are merged into one cluster. Finally, all objects are merged into one cluster, completely. Whereas, merging into one cluster is not adaptive for the actual situation. Hence, the clustering finish time can be controlled with appropriate termination condition. Compared with other typical clustering algorithms used in the image segmentation, such as K-means [19] and fuzzy C-means [20], HCA can acquire satisfactory results without prior information of cluster number, which is more adaptive for the SAR image segmentation.

After the inverse mapping, the equivalent data can be obtained for the ISAR processing. For ship targets with complicated motions, the imaging quality can be improved via the ISAR motion compensation and Range-Instantaneous Doppler (RID) algorithm [21]–[24]. First, the identical movement of all scatterers can be compensated by the motion compensation [25]. After that, the processed data can be analyzed by the time-frequency distribution (TFD) [25]–[28]. Then, after selecting the imaging moments, the instantaneous ISAR images can be yielded [29]–[32]. In this article, the TFD we choose is the smoothed pseudo Wigner-Ville distribution (SPWVD), which can give consideration to both the time-frequency resolution and cross-term suppression.

The remained constructions of this article are as follows. The echo signal is modeled and SAR processing approach via the 2-D spectrum of echo is introduced in Section II. On this basis, the residual phase of the processed signal is analyzed. Additionally, in Section III, the proposed automatic ISAR refocusing approach is presented in detail, including the automatic SAR image segmentation approach, inverse mapping and ISAR refocusing algorithm. Moreover, in Section IV, the computational complexity of the presented method is analyzed. Furthermore, in Section V, simulated and real measured data are processed to
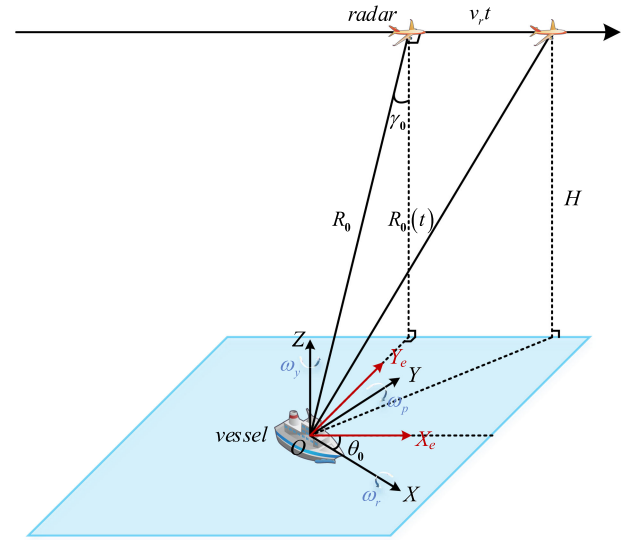

Fig. 1. Geometry of hybrid imaging scene.

yield imaging results for verifying the validity of the presented method. Eventually, the conclusion is drawn in Section VI.

II. IMAGING GEOMETRY MODEL, SAR IMAGING PROCESSING AND ANALYSIS OF RESIDUAL PHASE

In this section, the geometry of hybrid imaging scene is modeled. Based on the geometry and practical circumstance, the range between the scatterer and radar is approximated as the second-order polynomial form. Then, the SAR processing method we adopt in this article is introduced. For attaining SAR image efficiently, we employ the SAR processing approach based on the echo's 2-D spectrum. On this basis, the residual phase of the processed signal after SAR imaging is analyzed to demonstrate the necessity of applying ISAR technique. Meanwhile, the reason of defocus in the SAR image is explained.

A. Imaging Geometry Model

Fig. 1 gives the geometry of hybrid imaging scene. The radar carried by an aircraft has a straight trajectory, a uniform velocity v_r and flight altitude H. The minimum distance between the centroid of ship and radar is R_0, and γ_0 denotes the depression angle. Then, the instantaneous range between the ship and radar can be represented as follows:

$$R_0(t_m) = \sqrt{R_0^2 + (v_r t_m)^2} \tag{1}$$

where t_m represents the slow time. On account of $v_r t_m \ll R_0$, the instantaneous range can be approximated as follows:

$$R_0(t_m) \approx R_0 + \frac{v_r^2}{2R_0} t_m^2. \tag{2}$$

Two coordinate systems are established as shown in Fig. 1. One is target coordinate system O-XYZ, where origin is the centroid of ship, X-axis is same as the direction of ship's bow and Z-axis is perpendicular to the sea surface. The other

is scene coordinate system $O\text{-}X_eY_eZ$, which can achieve via anticlockwise rotating $O\text{-}XYZ$ with θ_0 around the Z-axis. In the system $O\text{-}X_eY_eZ$, the X_e-axis is parallel to the direction of radar trajectory. Therefore, via coordinate transformation, the instantaneous coordinate of radar in the $O\text{-}X_eY_eZ$ can be transformed into the $O\text{-}XYZ$, that is

$$\begin{bmatrix} x_r\left(t_m\right) \\ y_r\left(t_m\right) \\ z_r\left(t_m\right) \end{bmatrix} = \begin{bmatrix} \cos\theta_0 & -\sin\theta_0 & 0 \\ \sin\theta_0 & \cos\theta_0 & 0 \\ 0 & 0 & 1 \end{bmatrix} \begin{bmatrix} v_r t_m \\ R_0 \sin\gamma_0 \\ H \end{bmatrix} \quad (3)$$

where $[x_r(t_m), y_r(t_m), z_r(t_m)]^T$ is the radar coordinate in the target coordinate system $O\text{-}XYZ$.

It is assumed that the ship on the sea surface exists rotations in the three directions (roll, yaw, and pitch), and rotations are approximatively regarded as sinusoidal rotating around X, Y, and Z-axes. Sinusoidal rotations can be represented as follows:

$$\theta_\xi\left(t_m\right) = \frac{1}{2}A_\xi \sin\left(2\pi\frac{t_m}{\tau_\xi} + \phi_\xi\right), \xi = r, p, y \quad (4)$$

where A_ξ denotes the amplitude of rotation, which is related to the sea condition, the type, velocity and course of ship; τ_ξ is the period of rotation related to the type of ship; ϕ_ξ signifies the initial phase of rotation; and r, p, and y represent roll, pitch, and yaw, respectively.

The rotation matrixes of three directions are as follows:

$$R_{\text{roll}}\left(t_m\right) = \begin{bmatrix} 1 & 0 & 0 \\ 0 & \cos\theta_r\left(t_m\right) & -\sin\theta_r\left(t_m\right) \\ 0 & \sin\theta_r\left(t_m\right) & \cos\theta_r\left(t_m\right) \end{bmatrix} \quad (5)$$

$$R_{\text{pitch}}\left(t_m\right) = \begin{bmatrix} \cos\theta_p\left(t_m\right) & 0 & -\sin\theta_p\left(t_m\right) \\ 0 & 1 & 0 \\ \sin\theta_p\left(t_m\right) & 0 & \cos\theta_p\left(t_m\right) \end{bmatrix} \quad (6)$$

$$R_{\text{yaw}}\left(t_m\right) = \begin{bmatrix} \cos\theta_y\left(t_m\right) & -\sin\theta_y\left(t_m\right) & 0 \\ \sin\theta_y\left(t_m\right) & \cos\theta_y\left(t_m\right) & 0 \\ 0 & 0 & 1 \end{bmatrix}. \quad (7)$$

Then, the target rotation matrix can be acquired by

$$R_t\left(t_m\right) = R_{\text{roll}}\left(t_m\right) \cdot R_{\text{pitch}}\left(t_m\right) \cdot R_{\text{yaw}}\left(t_m\right)$$

$$= \begin{bmatrix} h_{11}\left(t_m\right) & h_{12}\left(t_m\right) & h_{13}\left(t_m\right) \\ h_{21}\left(t_m\right) & h_{22}\left(t_m\right) & h_{23}\left(t_m\right) \\ h_{31}\left(t_m\right) & h_{32}\left(t_m\right) & h_{33}\left(t_m\right) \end{bmatrix}. \quad (8)$$

Exploiting the Taylor series expansion at $t_m = -\phi_\xi\tau_\xi/2\pi$, and retaining the terms lower than the third order, the $\cos(\theta_\xi(t_m))$ and $\sin(\theta_\xi(t_m))$ can be approximated as follows:

$$\cos\left(\theta_\xi\left(t_m\right)\right) \approx 1 - \pi^2\frac{A_\xi^2}{2\tau_\xi^2}\left(t_m + \frac{\phi_\xi\tau_\xi}{2\pi}\right)^2 \quad (9)$$

$$\sin\left(\theta_\xi\left(t_m\right)\right) \approx \pi\frac{A_\xi}{\tau_\xi}\left(t_m + \frac{\phi_\xi\tau_\xi}{2\pi}\right). \quad (10)$$

Accordingly, the terms $h_{ij}(t_m)$ in the target rotation matrix (8) can be approximated as follows:

$$h_{ij}\left(t_m\right) \approx C_{ij}t_m^2 + B_{ij}t_m + A_{ij} \quad (11)$$

where C, B, and A represent the second order, the first-order coefficient, and the constant term, respectively; and $i, j = 1, 2, 3$.

Meanwhile, the ship target moves forward with a uniform velocity v. Assuming that there is a scatterer P on the ship, at the initial moment, the coordinate of scatterer P is $[x_p, y_p, z_p]^T$. Moving with ship target, the position of scatterer P at the moment t_m can be represented as follows:

$$\begin{bmatrix} x_p\left(t_m\right) \\ y_p\left(t_m\right) \\ z_p\left(t_m\right) \end{bmatrix} = R_t\left(t_m\right)\begin{bmatrix} x_p \\ y_p \\ z_p \end{bmatrix} + \begin{bmatrix} vt_m \\ 0 \\ 0 \end{bmatrix}. \quad (12)$$

Consequently, at the moment t_m, the range between the radar and scatterer P can be calculated as follows:

$$R_p\left(t_m\right) = \Big[\left(x_p\left(t_m\right) - x_r\left(t_m\right)\right)^2$$

$$+ \left(y_p\left(t_m\right) - y_r\left(t_m\right)\right)^2 + \left(z_p\left(t_m\right) - z_r\left(t_m\right)\right)^2\Big]^{\frac{1}{2}}$$

$$= \Big[R_0(t_m)^2 + r_p(t_m)^2 - 2x_p\left(t_m\right)x_r\left(t_m\right)$$

$$- 2y_p\left(t_m\right)y_r\left(t_m\right) - 2z_p\left(t_m\right)z_r\left(t_m\right)\Big]^{\frac{1}{2}} \quad (13)$$

where $R_0(t_m)^2 = x_r(t_m)^2 + y_r(t_m)^2 + z_r(t_m)^2$, and the displacement of the ship can be represented as $r_p(t_m)^2 = x_p(t_m)^2 + y_p(t_m)^2 + z_p(t_m)^2$.

Owing to $r_p(t_m) \ll R_0(t_m)$, the range model in (13) can be approximated as follows:

$$R_p\left(t_m\right) \approx R_0\left(t_m\right)$$

$$- \frac{x_p\left(t_m\right)x_r\left(t_m\right) + y_p\left(t_m\right)y_r\left(t_m\right) + z_p\left(t_m\right)z_r\left(t_m\right)}{R_0\left(t_m\right)}$$

$$- \frac{\left[x_p\left(t_m\right)x_r\left(t_m\right) + y_p\left(t_m\right)y_r\left(t_m\right) + z_p\left(t_m\right)z_r\left(t_m\right)\right]^2}{2R_0(t_m)^3}. \quad (14)$$

Apparently, according to (2) and (11), the range history $R_p(t_m)$ can be expressed as follows:

$$R_p\left(t_m\right) \approx \rho_2 t_m^2 + \rho_1 t_m + \rho_0 \quad (15)$$

where ρ_2, ρ_1, and ρ_0 are range parameters.

B. Signal Model and SAR Processing

The radar transmits the linear frequency modulation signal, and the baseband signal can be expressed as follows:

$$s_t\left(\hat{t}\right) = a_r\left(\hat{t}\right)\exp\left(j\pi\gamma\hat{t}^2\right) \quad (16)$$

where $a_r(\hat{t})$ is the envelope of transmitting signal, $\hat{t}$ represents the fast time, and γ denotes the frequency modulation ratio.

The baseband echo of the scatterer P can be represented as follows:

$$s_r\left(\hat{t}, t_m\right) = a_r\left(\hat{t} - \frac{2R_p\left(t_m\right)}{c}\right) a_a\left(t_m\right)$$

$$\cdot \exp\left[j\pi\gamma\left(\hat{t} - \frac{2R_p\left(t_m\right)}{c}\right)^2\right]$$

$$\times \exp\left[-j\frac{4\pi}{\lambda}R_p\left(t_m\right)\right] \tag{17}$$

where $\lambda = c/f_c$ is the signal's wavelength, f_c represents the carrier frequency, c is the light velocity, $R_p(t_m)$ is the range between the scatterer P and radar, and $a_a(t_m)$ is the window function along the azimuth direction. Based on (15), $R_p(t_m)$ can be shown as follows:

$$R_p\left(t_m\right) = \rho_2 t_m{}^2 + \rho_1 t_m + \rho_0. \tag{18}$$

Hence, the round trip range $RR_p(t_m)$ is

$$RR_p\left(t_m\right) = \mu_2 t_m{}^2 + \mu_1 t_m + \mu_0 \tag{19}$$

where $\mu_i(i = 0, 1, 2)$ denotes $2\rho_i$.

To generate high-quality SAR images, the echo signal needs to be compensated by SAR imaging algorithm [33]. In this article, the SAR processing method based on the 2-D spectrum of echo is adopted for efficient imaging. The employed SAR approach can be summarized as follows.

1) The echo signal is implemented Fourier transform (FT) along the fast time.
2) Then, the signal is implemented FT along the slow time, i.e., obtaining the 2-D spectrum of echo.
3) According to the 2-D spectrum, the compensation functions can be constructed.
4) With multiplying echo signal by compensation functions and implementing inverse FT (IFT) in the range and azimuth direction, the well-focused SAR image will be generated.

First, by FT along the fast time $\hat{t}$, the baseband echo in (17) can be transformed into the $f_r - t_m$ domain as follows:

$$s_r\left(f_r, t_m\right) = a_r\left(f_r\right) a_a\left(t_m\right)$$

$$\cdot \exp\left(-j\pi\frac{f_r^2}{\gamma}\right) \exp\left[-j\frac{2\pi}{c}RR_p\left(t_m\right)\left(f_r + f_c\right)\right]. \tag{20}$$

Then, the 2-D spectrum can be obtained by FT along the slow time. Obviously, the FT along the slow time can be solved by the principle of stationary phase. Moreover, it can be observed that there is a single-frequency signal in (20), that is $\exp[-j2\pi(\mu_1(f_r + f_c)/c)t_m]$. Via applying the frequency shift property of Fourier transform, the derivation process will be further simplified.

It is supposed that $RR_{p1}(t_m) \approx \mu_2 t_m^2 + \mu_0$, then the echo signal can be shown as follows:

$$s_{p1}\left(\hat{t}, t_m\right) = a_r\left(\hat{t} - \frac{RR_{p1}\left(t_m\right)}{c}\right) a_a\left(t_m\right)$$

$$\cdot \exp\left[j\pi\gamma\left(\hat{t} - \frac{RR_{p1}\left(t_m\right)}{c}\right)^2\right]$$

$$\times \exp\left[-j\frac{2\pi}{\lambda}RR_{p1}\left(t_m\right)\right]. \tag{21}$$

After FT along the fast time $\hat{t}$, the signal in the $f_r - t_m$ domain can be acquired, that is

$$s_{p1}\left(f_r, t_m\right) = a_r\left(f_r\right) a_a\left(t_m\right)$$

$$\cdot \exp\left(-j\pi\frac{f_r^2}{\gamma}\right)$$

$$\times \exp\left[-j\frac{2\pi}{c}RR_{p1}\left(t_m\right)\left(f_r + f_c\right)\right] \tag{22}$$

where f_r denotes the frequency corresponding to the fast time.

Afterward, via FT along the slow time t_m, the signal in the $f_r - f_a$ domain can be obtained. The phase term of Fourier integral can be expressed as follows:

$$\phi_{p1}\left(t_m\right) = -\frac{2\pi}{c}\left(f_r + f_c\right)\left(\mu_2 t_m^2 + \mu_0\right) - 2\pi f_a t_m \tag{23}$$

where f_a represents the Doppler frequency. Then, the first-order derivative of phase (23) with respect to the slow time is

$$\phi'_{p1}\left(t_m\right) = -\frac{2\pi}{c}\left(f_r + f_c\right) 2\mu_2 t_m - 2\pi f_a. \tag{24}$$

When $\phi'_{p1}(t_m) = 0$, the point of stationary phase $t_m^*(f_a)$ can be attained as follows:

$$t_m^*\left(f_a\right) = -\frac{c}{2\mu_2\left(f_r + f_c\right)} f_a. \tag{25}$$

Substituting (25) into (23), the 2-D spectrum of signal $s_{p1}(f_r, t_m)$ can be acquired as follows:

$$s_{p1}\left(f_r, f_a\right) = a_r\left(f_r\right) a_a\left(f_a\right) \exp\left[\varphi_{p1}\left(f_r, f_a\right)\right] \tag{26}$$

where the form of phase $\varphi_{p1}(f_r, f_a)$ is

$$\varphi_{p1}\left(f_r, f_a\right) = -\pi\frac{f_r^2}{\gamma} + \frac{\pi c}{2\mu_2\left(f_r + f_c\right)} f_a^2 - \frac{2\pi\mu_0}{c}\left(f_r + f_c\right). \tag{27}$$

After acquiring the 2-D spectrum of $s_{p1}(\hat{t}, t_m)$, the expression of $s_r(f_r, f_a)$ can be obtained by the characteristics of FT [33]. For the signal $s_{p1}(f_r, t_m)$, the process of solving 2-D spectrum can be represented as follows:

$$s_{p1}\left(f_r, t_m\right) \xrightarrow{\text{FT}} s_{p1}\left(f_r, f_a\right). \tag{28}$$

The process of solving 2-D spectrum for (20) can be represented as follows:

$$s_r\left(f_r, t_m\right) \xrightarrow{\text{FT}} s_r\left(f_r, f_a\right). \tag{29}$$

There is a relationship between $s_r(f_r, t_m)$ and $s_{p1}(f_r, t_m)$, that is

$$s_r\left(f_r, t_m\right) = s_{p1}\left(f_r, t_m\right) \cdot \exp\left[-j\frac{2\pi}{c}\mu_1\left(f_r + f_c\right)t_m\right]. \tag{30}$$

Then, according to (30), the process in (29) is equivalent to

$$s_{p1}\left(f_r, t_m\right)\exp\left[-j\frac{2\pi}{c}\mu_1\left(f_r + f_c\right)t_m\right]$$

$$\xrightarrow{\text{FT}} s_{p1}\left(f_r, f_a + \mu_1\frac{f_r + f_c}{c}\right). \tag{31}$$

Hence, by substituting $f_a + \mu_1(f_r + f_c)/c$ for f_a in (27), the 2-D spectrum of $s_r(\hat{t}, t_m)$ is

$$s_r\left(f_r, f_a\right) = a_r\left(f_r\right)a_a\left(f_a\right)\exp\left[\phi\left(f_r, f_v\right)\right] \tag{32}$$

where $\phi(f_r, f_a)$ is

$$\phi\left(f_r, f_a\right) = \frac{\pi c}{2\mu_2\left(f_r + f_c\right)}f_a^2$$
$$+ \frac{\pi\mu_1}{\mu_2}f_a + \left(\frac{\pi\mu_1^2}{2c\mu_2} - \frac{2\pi\mu_0}{vc}\right)\left(f_r + f_c\right) - \pi\frac{f_r^2}{\gamma}. \tag{33}$$

Due to $f_r \ll f_c$, the phase $\phi(f_r, f_a)$ can be approximated as follows:

$$\phi\left(f_r, f_a\right) = \phi_2\left(f_a\right)f_r^2 + \phi_1\left(f_a\right)f_r + \phi_0\left(f_a\right) \tag{34}$$

where $\phi_2(f_a)$, $\phi_1(f_a)$, and $\phi_0(f_a)$ are as follows:

$$\phi_2\left(f_a\right) = \frac{\pi c}{2\mu_2 f_c^3}f_a^2 - \frac{\pi}{\gamma} \tag{35}$$

$$\phi_1\left(f_a\right) = -\frac{\pi c}{2\mu_2 f_c^2}f_a^2 + \frac{\pi\mu_1^2}{2c\mu_2} - \frac{2\pi\mu_0}{c} \tag{36}$$

$$\phi_0\left(f_a\right) = \frac{\pi c}{2\mu_2 f_c}f_a^2 + \frac{\pi\mu_1}{\mu_2}f_a + \left(\frac{\pi\mu_1^2}{2c\mu_2} - \frac{2\pi\mu_0}{c}\right)f_c. \tag{37}$$

As can be seen from (34) to (36), the frequency f_r and Doppler frequency f_a exist coupling phenomena. Meanwhile, there is a quadratic term of Doppler frequency f_a in (37). Hence, the 2-D spectrum of echo exists the 2-D broadening.

Fig. 2 gives the flowchart of SAR processing approach. The detailed procedures are as follows.

1) Initially, the echo is transformed into the $f_r - f_a$ domain by the 2-D FT.
2) With the static scatterer in the center of scene as reference, the 2-D decoupling function and pulse compression function in the range are constructed as follows:

$$H_1\left(f_r, f_a\right) = \exp\left[-j\phi_1\left(f_a\right)f_r\right] \tag{38}$$

$$H_2\left(f_r, f_a\right) = \exp\left[-j\phi_2\left(f_a\right)f_r^2\right]. \tag{39}$$

Multiplying the 2-D spectrum with (38) and (39), the signal in the $\hat{t} - f_a$ domain is attained via IFT with respect to $\hat{t}$, which is expressed as follows:

$$s\left(\hat{t}, f_a\right)$$
$$= \mathrm{sinc}\left[B_r\left(\hat{t} - \frac{2\left(\rho_0 - R_0\right)}{c}\right)\right]a_a\left(f_a\right)\exp\left[j\phi_0\left(f_a\right)\right] \tag{40}$$

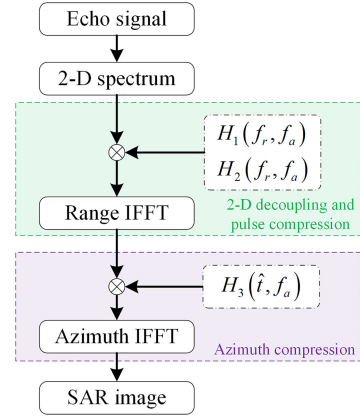where B_r is the bandwidth of the signal.

Fig. 2. Flowchart of the SAR processing approach.

3) Accordingly, the azimuth compression function is constructed as follows:

$$H_3\left(\hat{t}, f_a\right) = \exp\left[-j\phi_0\left(f_a\right)\right]. \tag{41}$$

Using the IFT with respect to t_m, we can attain the SAR image by

$$s\left(\hat{t}, t_m\right) = \mathrm{sinc}\left[B_r\left(\hat{t} - \frac{2\left(\rho_0 - R_0\right)}{c}\right)\right]\mathrm{sinc}$$
$$\times\left[\Delta f_a\left(t_m - \frac{x_p}{v_r}\right)\right]. \tag{42}$$

where $\mathrm{sinc}(\cdot)$ is sinc function.

Hence, the sinc cannot separate from $\left[\Delta f_a\left(t_m - \frac{x_p}{v_r}\right)\right]$.

This SAR processing method has some advantages and limitations [33]. First, compared with other SAR algorithms, this SAR algorithm compensates the echo in the frequency domain, which brings high efficiency to SAR imaging. Moreover, the SAR compensation functions are constructed according to the 2-D spectrum of echo, which can ensure the high accuracy of SAR algorithm. Nevertheless, the compensation functions are related to parameters of the scene center. Hence, when the imaging scene has a large width, the performance of SAR compensation may be decreased. Under the circumstance, block processing along the range direction can solve this problem.

C. Analysis of the Residual Phase

Owing to the difficulty of measuring target motion parameters, in the practical circumstance, the range parameters $\rho_i(i = 0, 1, 2)$ of stationary target in the scene center will be utilized for the SAR processing, which results in a blurring of SAR image to some extent. Hence, the necessity of employing ISAR technique is illustrated via deducing and analyzing the residual phase of signal after SAR compensation.

If the target is stationary, according to (2), the range parameters can be denoted as $\tilde{\rho}_2 = v_r^2/2R_0$, $\tilde{\rho}_1 = 0$, and $\tilde{\rho}_0 = R_0$. Meanwhile, the range parameters of the moving target are signified as $\rho_i(i = 0, 1, 2)$, which can also be represented as $\rho_i = \tilde{\rho}_i + \Delta\rho_i$. Considering the parameters $\mu_i = 2\rho_i$, μ_i can be denoted as $\mu_i = \tilde{\mu}_i + \Delta\mu_i$.

Based on (34)–(37), the phase term of echo's 2-D spectrum is

$$\phi(f_r, f_a) = \left[-\frac{\pi}{\gamma} + \frac{\pi c}{2(\tilde{\mu}_2 + \Delta\mu_2) f_c^3} f_a^2 \right] f_r^2$$
$$+ \left[\frac{\pi(\tilde{\mu}_1 + \Delta\mu_1)^2}{2(\tilde{\mu}_2 + \Delta\mu_2) c} - \frac{\pi c}{2(\tilde{\mu}_2 + \Delta\mu_2) f_c^2} f_a^2 \right.$$
$$\left. - \frac{2\pi(\tilde{\mu}_0 + \Delta\mu_0)}{c} \right] f_r + \phi_0(f_a). \quad (43)$$

According to (38) and (39), using the range parameters $\tilde{\rho}_i (i = 0, 1, 2)$, the 2-D spectrum of echo can be compensated by the phase compensation function as follows:

$$\phi_{\text{com}}(f_r, f_a) = \left(-\frac{\pi}{\gamma} + \frac{\pi c}{2\tilde{\mu}_2 f_c^3} f_a^2 \right) f_r^2$$
$$+ \left(\frac{\pi\tilde{\mu}_1^2}{2\tilde{\mu}_2 c} - \frac{\pi c}{2\tilde{\mu}_2 f_c^2} f_a^2 - \frac{2\pi\tilde{\mu}_0}{c} \right) f_r. \quad (44)$$

After compensation, the signal's 2-D spectrum phase is

$$\phi_{\text{res}}(f_r, f_a) = \phi(f_r, f_a) - \phi_{\text{com}}(f_r, f_a)$$
$$= \phi_{\text{res},2}(f_a) f_r^2 + \phi_{\text{res},1}(f_a) f_r + \phi_0(f_a) \quad (45)$$

where $\phi_{\text{res},2}(f_a)$ and $\phi_{\text{res},1}(f_a)$ are

$$\phi_{\text{res},2}(f_a) = -\frac{\pi c \Delta\mu_2}{2\tilde{\mu}_2(\tilde{\mu}_2 + \Delta\mu_2) f_c^3} f_a^2 \quad (46)$$

and

$$\phi_{\text{res},1}(f_a) = \frac{\pi c \Delta\mu_2}{2\tilde{\mu}_2(\tilde{\mu}_2 + \Delta\mu_2) f_c^2} f_a^2 - \frac{\pi\tilde{\mu}_1^2 \Delta\mu_2}{2\tilde{\mu}_2(\tilde{\mu}_2 + \Delta\mu_2) c}$$
$$+ \frac{\pi\left(2\tilde{\mu}_1\Delta\mu_1 + (\Delta\mu_1)^2\right)}{2(\tilde{\mu}_2 + \Delta\mu_2) c} - \frac{2\pi\Delta\mu_0}{c}. \quad (47)$$

On the basis of (45)–(47), the quadratic term of f_r and the couple of f_a and f_r result in the defocusing of SAR images in the range dimension.

By transforming the signal into the $\hat{t} - f_a$ domain, the phase term of signal can be derived according to (37) and (40), which can be expressed as follows:

$$\phi_0(f_a) = \frac{\pi c}{2f_c(\tilde{\mu}_2 + \Delta\mu_2)} f_a^2 + \frac{\pi(\tilde{\mu}_1 + \Delta\mu_1)}{\tilde{\mu}_2 + \Delta\mu_2} f_a$$
$$+ \left[\frac{\pi(\tilde{\mu}_1 + \Delta\mu_1)^2}{2(\tilde{\mu}_2 + \Delta\mu_2) c} - \frac{2\pi}{c}(\tilde{\mu}_0 + \Delta\mu_0) \right] f_c. \quad (48)$$

In accordance with (37) and (41), the phase compensation function is

$$\phi_{\text{com},0}(f_a) = \frac{\pi c}{2\tilde{\mu}_2 f_c} f_a^2 + \frac{\pi\tilde{\mu}_1}{\tilde{\mu}_2} f_a + \left(\frac{\pi\tilde{\mu}_1^2}{2\tilde{\mu}_2 c} - \frac{2\pi}{c}\tilde{\mu}_0 \right) f_c. \quad (49)$$

After compensation, the residual phase of signal is

$$\phi_{\text{res},0}(f_a) = \phi_0(f_a) - \phi_{\text{com},0}(f_a)$$
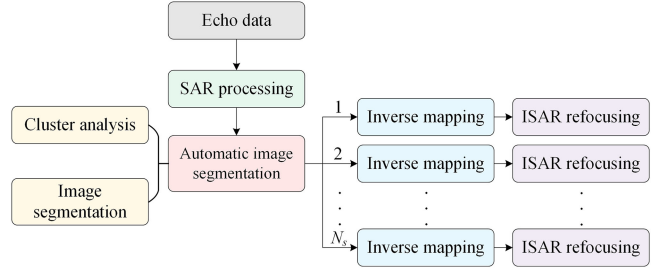$$= -\frac{\pi c \Delta\mu_2}{2f_c\tilde{\mu}_2(\tilde{\mu}_2 + \Delta\mu_2)} f_a^2$$

Fig. 3. Flowchart of the proposed approach in this article.

$$+ \left[\frac{\pi\Delta\mu_1}{\tilde{\mu}_2 + \Delta\mu_2} - \frac{\pi\tilde{\mu}_1\Delta\mu_2}{\tilde{\mu}_2(\tilde{\mu}_2 + \Delta\mu_2)} \right] f_a$$
$$+ \frac{2\pi f_c}{c} \left[\frac{-\tilde{\mu}_1^2\Delta\mu_2 + \tilde{\mu}_2\left(2\tilde{\mu}_1\Delta\mu_1 + (\Delta\mu_1)^2\right)}{4\tilde{\mu}_2(\tilde{\mu}_2 + \Delta\mu_2)} - \Delta\mu_0 \right]. \quad (50)$$

Obviously, there is a quadratic term of Doppler frequency f_a in (50), which leads to the azimuth defocusing of SAR images.

In addition, using the range parameter of stationary target in the scene center, the SAR processing cannot compensate the movements of ship targets. In order to acquire the well-focused images, the ISAR refocusing technique can be utilized for improving the quality of SAR images.

III. AUTOMATIC IMAGE SEGMENTATION AND ISAR REFOCUSING TECHNIQUE

In this section, a valid and labor-saving automatic hybrid imaging method is presented in detail, containing automatic image segmentation based on the clustering algorithm, inverse mapping, and ISAR refocusing. The clustering algorithm we adopt in the automatic image segmentation is agglomerative HCA. One of the advantages is that there is no need to know the number of categories in advance, which enlarges the application area and is appropriate to automatic hybrid imaging. Afterward, the method of data extraction is introduced, by which the equivalent data for the ISAR processing can be obtained. Accordingly, the procedures of ISAR refocusing processing are presented, including the motion compensation and RID algorithm.

The flowchart of the proposed approach in this article is exhibited in Fig. 3.

A. Automatic Image Segmentation and Inverse Mapping

Given that the SAR processing cannot thoroughly compensate the movements of ship targets, the ISAR refocusing technique can be utilized for enhancing the quality of SAR images. Since the movements of ships are usually different, the ISAR refocusing processing cannot be directly implemented. Consequently, before the ISAR refocusing, the SAR image segmentation method should be implemented to attain images of each ship target. Afterward, the equivalent data of each ship target can be obtained via inverse mapping. Then, the ISAR refocusing

technique can be applied to generate ISAR images. Whereas, the existing SAR image segmentation algorithms and inverse mapping procedure generally adopt the manual method, which will consume numerous human resources. In this article, an automatic ISAR refocusing method will be put forward to solve this problem.

Evidently, in the SAR image, pixels of each ship target are concentrated within a certain range and azimuth area. Hence, the clustering algorithm can be utilized for attaining the 2-D scopes of ships. According to the 2-D scopes of single target, a 2-D filter can be designed to eliminate the interference of other targets. Assuming that the SAR image and the 2-D filter are denoted as $I(x,y)$ and $F(x,y)$, respectively, the filtered SAR image $I_{n_s}(x,y)$ can be generated through

$$I_{n_s}(x,y) = I(x,y) \times F(x,y) \tag{51}$$

where the 2-D filter is

$$F(x,y) = \begin{cases} 1, & x = x_l, \ldots, x_h, y = y_l, \ldots, y_h \\ 0, & \text{others} \end{cases}. \tag{52}$$

N_s is the number of ship targets, n_s is the order ($n_s = 1, 2, \ldots, N_s$), x and y are the range and cross-range bin, x_l and y_l are the minimum order of x and y, x_h and y_h are the maximum order of x and y, respectively. Accordingly, the equivalent data domain will be attained by the IFT with respect to the azimuth bins. Afterward, via the ISAR refocusing technique, the clear and well-focused images can be obtained.

The basic procedures of automatic SAR image segmentation method and the data extraction are shown as follows.

1) Setting appropriate threshold, the binary image processing is employed to extract indexes of all ships' pixels in the SAR images.
2) Then, the ship pixels are classified by the appropriate clustering algorithm.
3) After clustering, the indexes of each ship's pixels can be obtained and the 2-D scopes of each ship can be attained meanwhile.
4) Based on the 2-D scopes, the 2-D filters can be designed to filter the SAR image and acquire the images containing only one ship target.
5) Finally, the equivalent data can be attained by the IFT with respect to the azimuth dimension, that is the inverse mapping.

The flowchart of extracting single ship target's equivalent ISAR data is exhibited in Fig. 4.

Remark 1: In the procedure 1), we employ the OTSU method to achieve the optimal threshold in the binary image processing. OTSU is an automatic and stable method of selecting optimal threshold. It divides the gray-level image into two parts: background and objects. Then, the "goodness" of threshold is evaluated by the standard of between-class variance, which can ensure the probability of error classification reaching minimum [34]. Owing to its simplification, automation and stabilization, OTSU widely applies in the area of image processing.
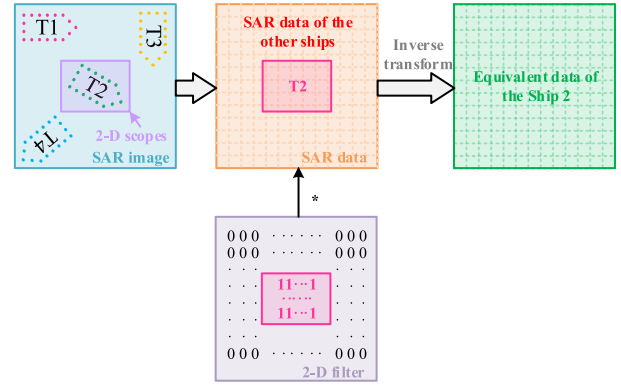

Fig. 4. Flowchart of extracting single ship target's equivalent ISAR data.

B. Agglomerative Hierarchical Clustering Algorithm

The clustering algorithms which we are familiar with are the K-means algorithm, fuzzy C-means, etc. However, these clustering algorithms are restricted in many applications because they generally require the number of categories in advance and severely affected by the initial values. Therefore, based on the advantage that it is no need for the prior number of the clusters, the agglomerative HCA is employed in this article to extract 2-D scopes of each target.

Initially, the agglomerative HCA regards each object as different cluster. Assuming that N objects wait for classification, there are N clusters in the beginning. Then, by calculating the distance matrix, the most similar or the nearest two clusters will be merged as one cluster. It is worth mentioning that there is a large amount of methods for calculating the distance in the HCA, for instance, the complete-linkage (maximum), single-linkage (minimum), and so on. Finally, by setting the appropriate threshold, the algorithm can be terminated and all objects will accomplish clustering.

The flowchart of HCA and automatic ISAR refocusing method is provided in Fig. 5.

The procedures of agglomerative single-linkage HCA are shown as follows.

1) Inputting the indexes of N objects and initializing the distance matrix $D_{N \times N}$. The threshold T_H is set to control the number of clusters.
2) Calculating the distances $D(i,j)$ between each object and other objects. The minimum distance can be searched and denoted as $D_{\min}$. The index of $D_{\min}$ is signified as (p_x, p_y).
3) Comparing $D_{\min}$ and $T_H D_{\max}$: if $D_{\min} \leq T_H D_{\max}$, the p_xth and the p_yth object are merged into one cluster, which is denoted as $[p_x; p_y]$, then the step 4) can be implemented. Otherwise, the process of HCA is terminated.
4) Updating the distance matrix $D_{N \times N}$: the rules are deleting the p_xth and p_yth row and column; adding a new row and columns p_{new} to record the distance between cluster $[p_x; p_y]$ and others, that is

$$\begin{cases} D(p_{\text{new}}, j) = \min\left(D(p_x, j), D(p_y, j)\right) \\ D(i, p_{\text{new}}) = D(p_{\text{new}}, i) \end{cases} \tag{53}$$
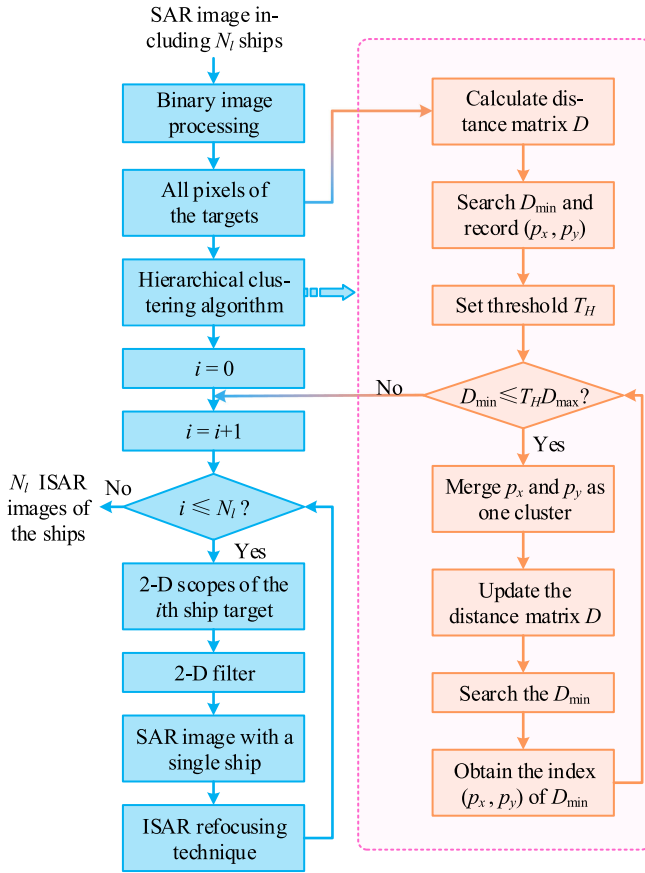
Fig. 5. Flowchart of HCA and automatic ISAR refocusing method.

where $i, j = 1, 2, \ldots, N$.

5) Calculating the minimum of the matrix $D_{N \times N}$ and recording the index of the minimum value as (p_x, p_y), then returning to the step 3).

C. ISAR Refocusing Technique

By utilizing the automatic SAR image segmentation, the SAR images containing individual ship target can be acquired. Accordingly, via the inverse mapping, the echo data equivalent to the ISAR data after range compression can be obtained. Given that the ship voyages on the sea surface, the movement of target can be decomposed into the identical movement of all scatterers and the diverse movement of each scatterer. The former can be compensated by the motion compensation technique of ISAR processing. The latter can be processed with the RID algorithm.

The motion compensation can compensate the identical movement of all scatterers. By using the range alignment, the moving trajectory of scatterer can be retained in one range bin. Here we implement the range alignment via minimizing the entropy of the average range profile in [35], which is a valid and precise approach. After phase compensating, the coherence of phase can be recovered. The phase correction method we adopt is the fast minimum entropy phase compensation (FMEPC)

proposed in [36]. FMEPC is an effective phase compensation approach via minimum entropy of the image.

The range alignment approach in [35] is a global optimization algorithm, which can also achieve satisfactory performance under the low signal noise ratio (SNR). This method can iteratively compute the offset of every range profile until its entropy reach the minimum value. Meanwhile, it has high efficiency owing to utilize fast Fourier transform (FFT). The average range profile can be defined as follows:

$$u_{\text{ave}}(r, \mathbf{\Delta_r}) = \sum_{n=0}^{N-1} u(r + \Delta_r(n), n) \tag{54}$$

where N_a is the number of azimuth bin, n and r are the orders of azimuth and range bin, respectively, $u(r, n)$ is range profile after range compensation, $\Delta_r(n)$ is the range offset of the nth range profile and $\mathbf{\Delta_r}$ is the range offset vector. By the time shift property of FT, $u_{\text{ave}}(r, \mathbf{\Delta_r})$ can be rewritten as follows:

$$u_{\text{ave}}(r, \mathbf{\Delta_r}) = \sum_{n=0}^{N-1} \int_{f_r} U(f_r, n) e^{j2\pi f_r \Delta_r(n)} \cdot e^{j2\pi f_r r} df_r \tag{55}$$

where $U(f_r, n)$ is the FT result of $u(r, n)$ along the range direction. The entropy of $u_{\text{ave}}(r, \mathbf{\Delta_r})$ can be calculated as follows:

$$E(\mathbf{\Delta_r}) = -\int_r \frac{u_{\text{ave}}(r, \mathbf{\Delta_r})}{S} \ln \frac{u_{\text{ave}}(r, \mathbf{\Delta_r})}{S} dr \tag{56}$$

where $S = \int_r u_{\text{ave}}(r, n) dr$ is the amplitude sum of $u_{\text{ave}}(r, n)$.

FMECP is a phase compensation approach based on the global optimization. Compared with other well-known methods, the FMEPC has advantages of high efficiency, high accuracy, and adapting under the low SNR. After range alignment, the signal of the nth pulse is denoted as $\mathbf{u}(r, n)$. The phase compensation procedure can be expressed as $\mathbf{u}'(n) = \mathbf{u}(n) \exp[-j\hat{\theta}(n)]$. For obtaining the optimized phase value, the entropy of ISAR image can be defined as follows:

$$E(I) = -\sum_p \sum_q \frac{|I(p, q)|^2}{S(I)} \ln \frac{|I(p, q)|^2}{S(I)} \tag{57}$$

where $I(p, q)$ represents the ISAR image, p and q are range and azimuth bin, the total energy of ISAR image can be calculated by $S(I) = \sum_p \sum_q |I(p, q)|^2$. Until the entropy achieves minimum value, the best focused ISAR image can be yielded. Hence, the optimized phase value should satisfy the following:

$$\hat{\theta}(n) = \arg\min_{\theta(n)} [E(I)]. \tag{58}$$

After motion compensation, the identical movement of scatters can be eliminated. Under the circumstance, the diverse motions of the scatters will produce the time-varying Doppler frequency, and make ISAR Range-Doppler (RD) images defocusing. Hence, the RID algorithm can be applied to deal with this problem in which echo signal is analyzed by the time-frequency distribution (TFD). Accordingly, the instantaneous ISAR image can be obtained by selecting appropriate imaging moment. In this article, the TFD we choose is the SPWVD, which can
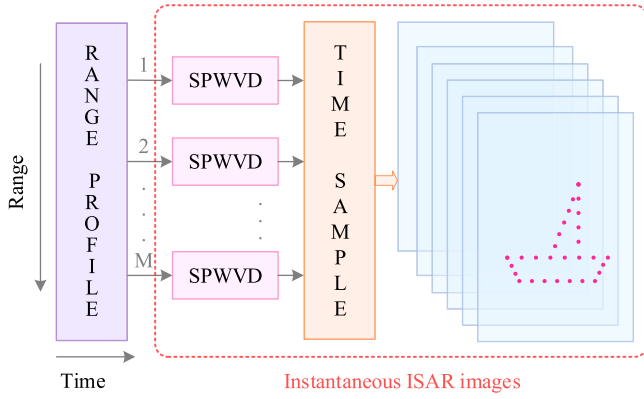
Fig. 6. Flowchart of RID algorithm based on the SPWVD.

achieve a better performance via smoothing both in time and frequency domain. SPWVD can be calculated via

$$\text{SPWVD}(t, f) = \int_{-\infty}^{+\infty} \int_{-\infty}^{+\infty}$$
$$g(u) h(\tau) s\left(t - u + \frac{\tau}{2}\right) s^*\left(t - u - \frac{\tau}{2}\right) e^{-j2\pi f\tau} \mathrm{d}u\mathrm{d}\tau \tag{59}$$

where $s(t)$ denotes the signal, $h(\tau)$ and $g(u)$ represent the real even window. The SPWVD gives consideration to the less cross-terms and high time-frequency resolution.

The process of RID algorithm via the SPWVD is exhibited in Fig. 6.

D. Comparison With Other State-of-the-Art Algorithms

In numerous state-of-the-art hybrid imaging algorithms, the procedures of image segmentation, inverse mapping, and ISAR refocusing are manual, which will limit the application in the practical imaging scenarios [4], [5], [8]. Furthermore, in the procedure of ISAR refocusing, these approaches usually utilize traditional RD algorithm, which will generate blurring RD images for the ship targets with complicated motions [4], [5], [8].

A novel ship target refocusing technique via the automatic image segmentation and ISAR RID technique is proposed in this article. The proposed algorithm automatically implements the processes of image segmentation, inverse mapping, and ISAR refocusing, which enlarges the range of application and overcomes the manual intervention. Moreover, taking ship targets with complicated motions into consideration, the instantaneous ISAR imaging method is employed, which will improve the quality of ISAR images.

IV. COMPUTATIONAL COMPLEXITY ANALYSIS

The proposed algorithm contains SAR imaging, automatic image segmentation, and ISAR refocusing. The computational complexity of calculating multiplication one time is represented as $O(1)$. In the SAR imaging process, first, the echo data is transformed into $f_r - f_a$ domain, i.e., FFT respecting to

azimuth and range dimension. This procedure costs the complexity of $O[N_a N_r(\log_2^{N_a} + \log_2^{N_r})/2]$. Then, the 2-D decoupling and pulse compression are implemented, which have a complexity of $O[N_a N_r(8 + \log_2^{N_r}/2)]$. Finally, the complexity of $O[N_a N_r(4 + \log_2^{N_a}/2)]$ is applied to achieve azimuth compression. Hence, the whole SAR imaging algorithm costs the complexity of $O[N_a N_r(12 + \log_2^{N_a} + \log_2^{N_r})]$.

In the automatic image segmentation, the HCA and inverse mapping are employed. It is supposed that N data or dataset are input into HCA and classified as k clusters. According to [37], the complexity of HCA is $O(kN^2)$. HCA classify data into k clusters, i.e., there are k ship targets in the SAR, which indicates inverse mapping will be implemented k times. Inverse mapping is consisted of 2-D filtering and IFFT in the azimuth direction. For one ship target, the complexities of 2-D filtering and IFFT are $O(4N_a N_r)$ and $O(N_a N_r \log_2^{N_a}/2)$, respectively. Therefore, applying automatic image segmentation costs complexity of $O[kN^2 + kN_a N_r(4 + \log_2^{N_a}/2)]$.

Given that SAR imaging processes echo data of large-scale scene and the data input into HCA are abundant, the complexity of the proposed algorithm almost depends on SAR imaging and automatic image segmentation. For ISAR refocusing procedure, it costs little complexity owing to the small scopes of azimuth and range, which can be ignored relatively.

The proposed algorithm has a good performance for ship imaging, whereas, the computational complexity is rather big, relatively. Fortunately, by deeply researching of clustering analysis, the modified and fast HCA and other excellent clustering algorithms have been emerged widely. Meanwhile, as the computing technology is developed rapidly, the efficiency of the presented approach will be enhanced sharply. In the future research, we will devote to study fast automatic imaging segmentation method.

V. EXPERIMENTAL RESULT

The simulated and real measured data are processed in this section. The imaging results will verify the availability of the hybrid imaging approach presented in this article.

A. Simulated Data

First, the simulated experiment is implemented to verify the availability of the hybrid SAR/ISAR processing method. The radar is carried by an aircraft, and parameters about the radar and imaging scene are shown in Table I. Each ship moves forward with a uniform velocity. Meanwhile, there are rotations in the three dimensions. Table II shows the movement parameters of ship targets.

The results of SAR processing are exhibited in Fig. 7. There are six ships in the scatterer model as shown in Fig. 7(a). The result of range compression can be observed in Fig. 7(b). Via the azimuth compression, the SAR image can be obtained in Fig. 7(c), from which the six ships can be recognized, while they have a little blurring. Hence, for improving the quality of images, the ISAR refocusing technique is required urgently.

TABLE I
PARAMETERS OF THE RADAR AND IMAGING SCENE

Parameters	Values
Bandwidth	60MHz
Carrier frequency	5.3GHz
Pulse width	10 μs
Velocity of the aircraft	49.5m/s
Height of the aircraft	3km
Squint angle	45 °
Pulse repetition frequency	500Hz
Length of the imaging scene	2km
Width of the imaging scene	1.2km
Synthetic aperture time	2.4241s

TABLE II
MOVEMENT PARAMETERS OF THE SHIPS

Ship number	Translational motion		Rotation		
	Velocity (m/s)	Direction θ_0 (°)	Amplitude A_ξ (°)	Average period (s)	Dimen-Sionality
1	10	0	5.00	26.4	Roll
2	10	105	0.90	11.2	Pitch
3	10	-90	1.33	33.0	Yaw
4	10	0	5.00	26.4	Roll
			0.90	11.2	Pitch
5	10	-120	5.00	26.4	Roll
			1.33	33.0	Yaw
6	10	-180	5.00	26.4	Roll
			0.90	11.2	Pitch
			1.33	33.0	Yaw

After yielding the SAR image, the agglomerative HCA is employed to achieve the 2-D scopes of ships. Results of the agglomerative HCA are observed in Fig. 8. Fig. 8(a) shows the result of binary image processing. Then, all indexes of ships' pixels in the SAR image can be obtained. Applying the agglomerative HCA, the indexes of ships' pixels are clustered into six clusters, which can be seen in Fig. 8(b).

After clustering, the 2-D scopes of six ship targets can be attained. Then, the automatic ISAR refocusing technique is executed to yield focused ISAR images. From Figs. 9–14, the imaging results of six ship targets are exhibited individually. Figs. 9–14 list imaging results of each ship target, in which there are: (a) SAR image, (b) the ISAR image with RD algorithm, (c) and (d) two refocused instantaneous ISAR images by RID method at different imaging moments. Obviously, the quality of refocused ISAR images is significantly higher.

Remark 2: The dependence of ISAR refocusing success on the rotation parameter can be illustrated as follows. The performance of ISAR refocusing is closely related to rotation parameter values. Under the low sea condition, the rotation parameter values are small, which causes small nonlinear phase terms in the azimuth direction. Hence, the ISAR refocusing method by the traditional RD method is an effective way under the low sea condition. Nevertheless, the effect of ISAR refocusing technique is influenced under the high sea condition. In this case, the rotation parameters are big. On one hand, under the severe sea condition, motions of ship targets are complicated, phenomenon of migration though resolution cell (MTRC) will
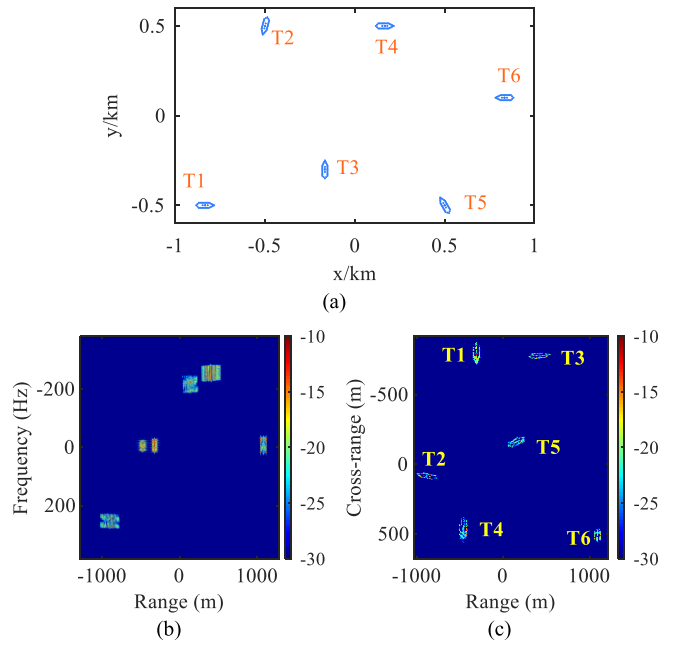

Fig. 7. Results of the SAR processing. (a) Model of scatterers. (b)Result of range compression. (c) SAR image.
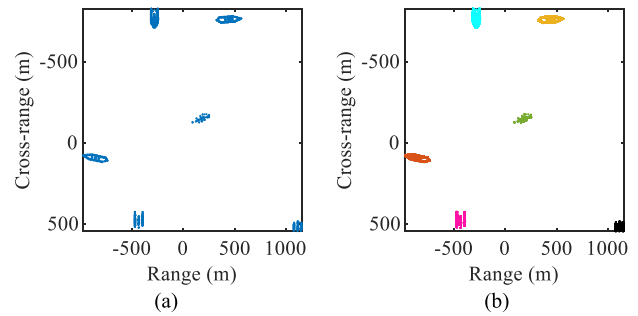

Fig. 8. Results of the agglomerative HCA. (a) Binary image of the SAR image. (b) Result of the HCA.

be sharply increasing. The influence by MTRC is difficult to compensation, which results in blurry imaging results. On the other hand, the imaging projection planes (IPPs) in imaging duration will change rapidly under the circumstance, which means the structure of scatterers projected on the IPP of ISAR changes continuously. It will bring about the unfocused ISAR images by the traditional methods. Fortunately, in this case, we can use the RID method to attain clear ISAR images.

B. Real Measured Data

To verify the availability of the presented hybrid imaging approach, the real measured airborne data about the ship targets on the sea surface is processed. The main parameters of radar system are listed in Table III. There are seven ships in the selected sea area. The results of SAR processing are shown in Fig. 15, where Fig. 15(a) is the result of range compression, and Fig. 15(b) is the SAR image with severe blurring.
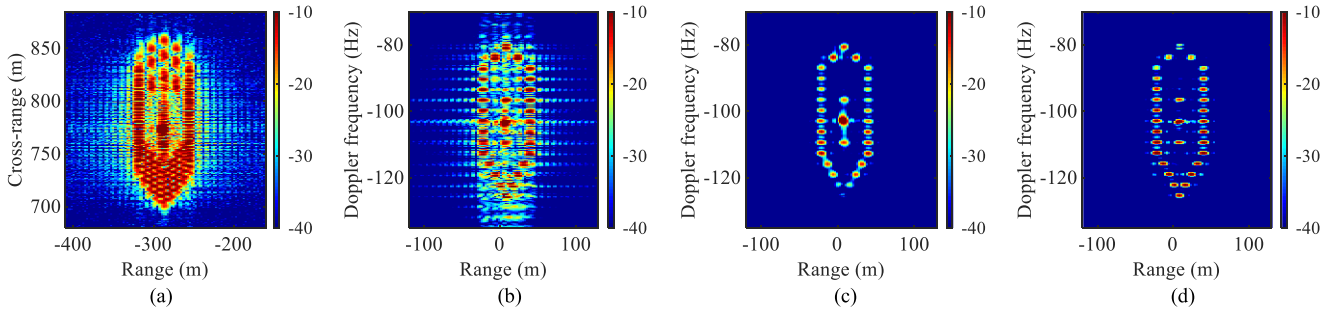
Fig. 9. Imaging results of the 1st ship target. (a) SAR image. (b) ISAR image with RD approach. (c) and (d) Refocused instantaneous ISAR images yielded by the RID approach.
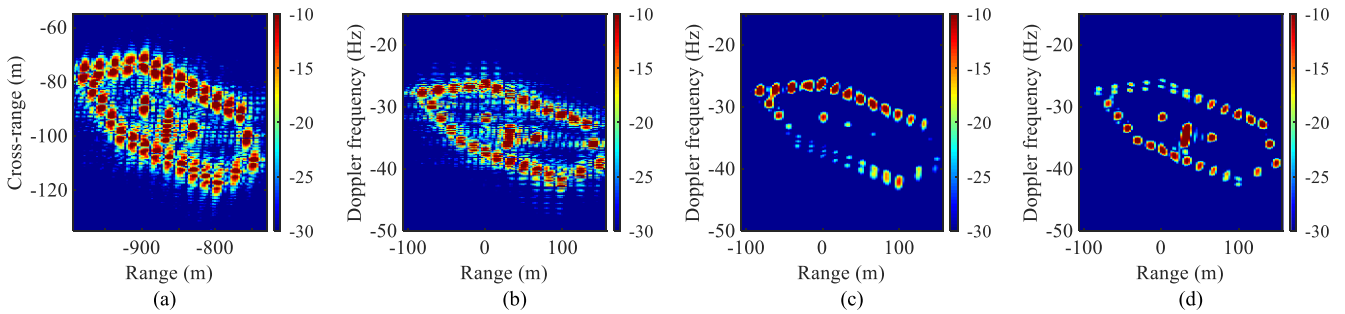

Fig. 10. Imaging results of the 2nd ship target. (a) SAR image. (b) ISAR image with RD approach. (c) and (d) Refocused instantaneous ISAR images yielded by the RID approach.
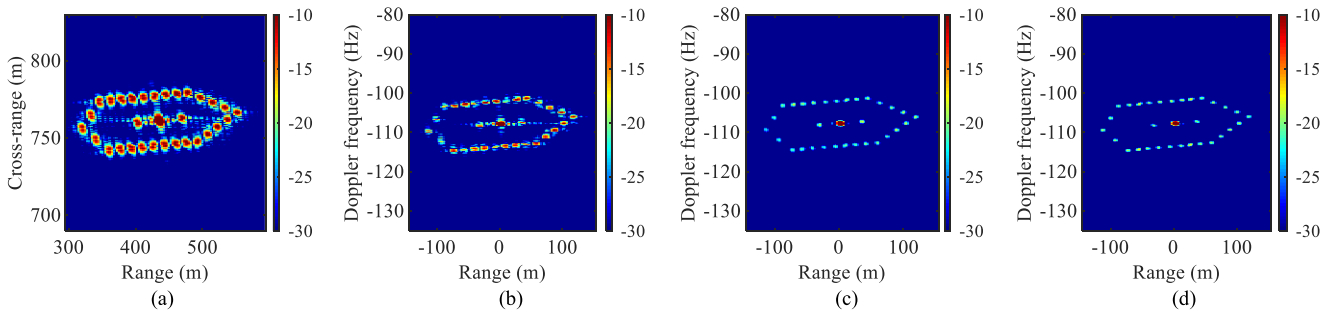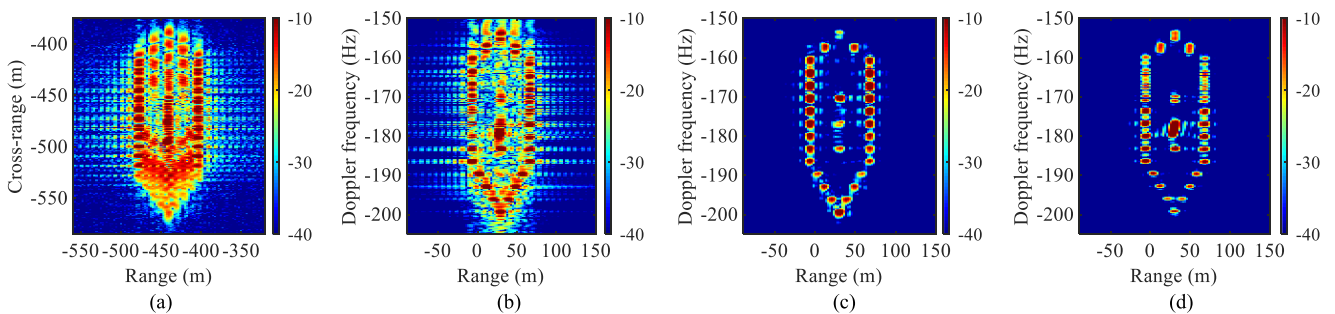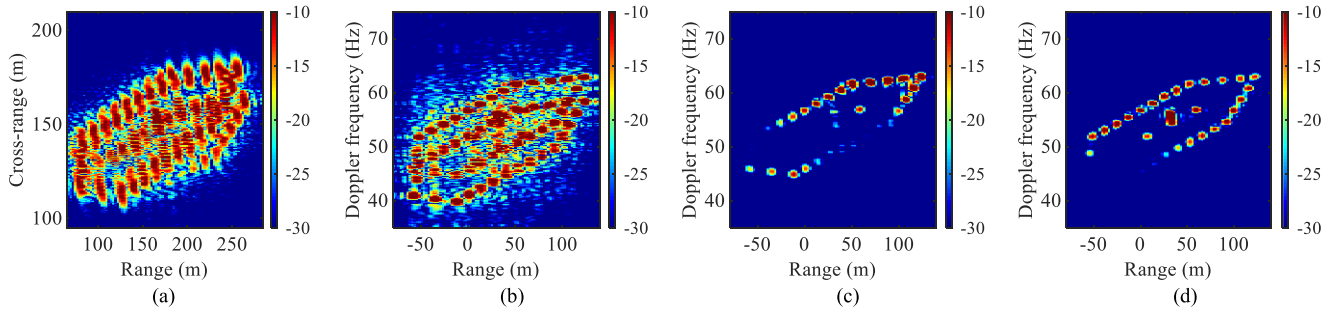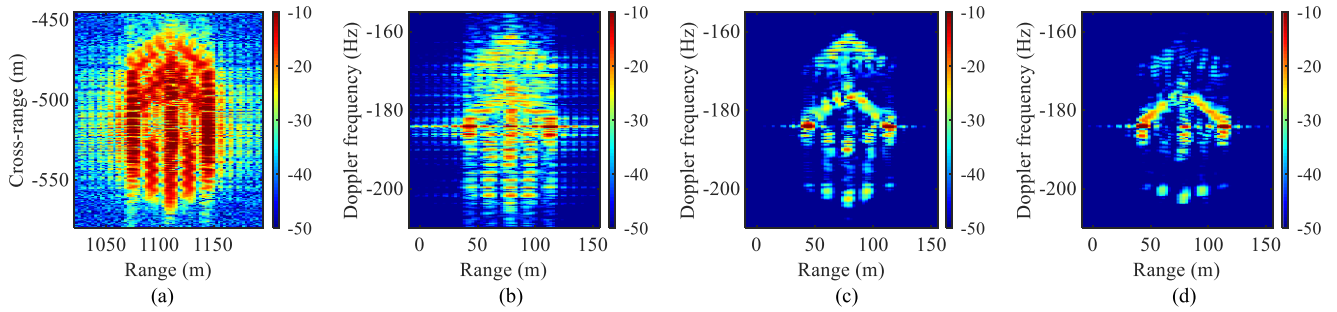

Fig. 11. Imaging results of the 3rd ship target. (a) SAR image. (b) ISAR image with RD approach. (c) and (d) Refocused instantaneous ISAR images yielded by the RID approach.

Fig. 12. Imaging results of the 4th ship target. (a) SAR image. (b) ISAR image with RD approach. (c) and (d) Refocused instantaneous ISAR images yielded by the RID approach.

Fig. 13.   Imaging results of the 5th ship target. (a) SAR image. (b) ISAR image with RD approach. (c) and (d) Refocused instantaneous ISAR images yielded by the RID approach.

Fig. 14.   Imaging results of the 6th ship target. (a) SAR image. (b) ISAR image with RD approach. (c) and (d) Refocused instantaneous ISAR images yielded by the RID approach.

TABLE III
PARAMETERS OF THE RADAR SYSTEM

Parameters	Values
Carrier frequency	5.3GHz
Bandwidth	60MHz
Pulse width	10 μs
Velocity of the aircraft	50.5m/s
Pulse repetition frequency	500Hz
Azimuth antenna aperture	2m
Synthetic aperture time	1.0594s
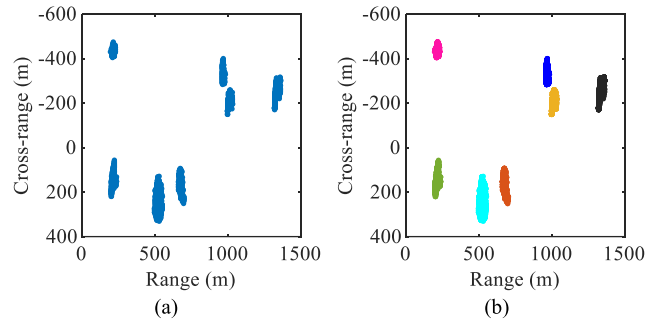
Fig. 16.   Results of the agglomerative HCA. (a) Binary image of SAR image. (b) Result of the HCA.

As observed in Fig. 16, after binary processing for the SAR image, the agglomerative HCA clusters objects as seven categories. According to the clustering results, each ship target is processed individually by the ISAR refocusing technique.

Imaging results of seven ship targets are listed in Figs. 17–23, where (a) shows the SAR image, (b) gives the ISAR image via RD algorithm, (c) and (d) are two instantaneous RID images. From Figs. 17–23, the image quality is enhanced significantly via ISAR refocusing technique.

Exploiting the RID algorithm, the focused effect in the azimuth direction will be improved distinctly. To testify this phenomenon, the azimuth profiles in some range bins of seven

Fig. 15.   Results of the SAR processing. (a) Result of range compression. (b) SAR image.
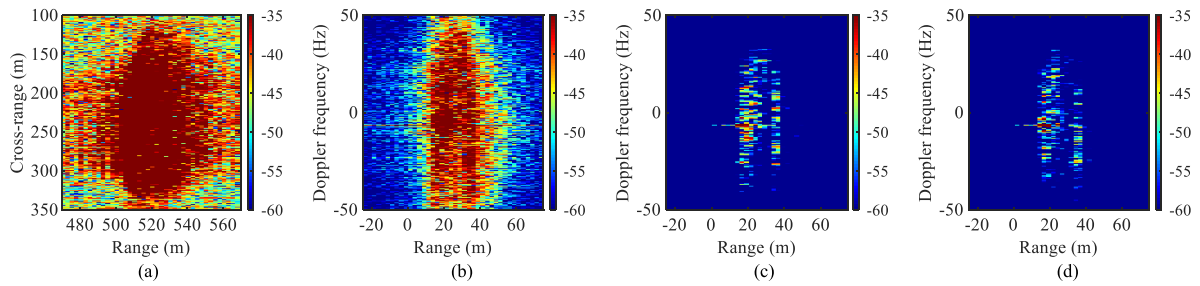
Fig. 17. Imaging results of the 1st ship target. (a) SAR image. (b) ISAR image with RD approach. (c) and (d) Refocused instantaneous ISAR images via the RID approach.
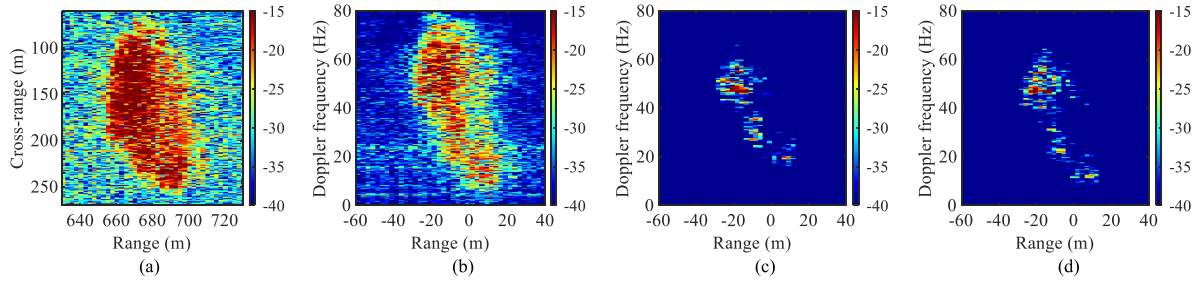

Fig. 18. Imaging results of the 2nd ship target. (a) SAR image. (b) ISAR image with RD approach, (c) and (d) refocused instantaneous ISAR images via the RID approach.
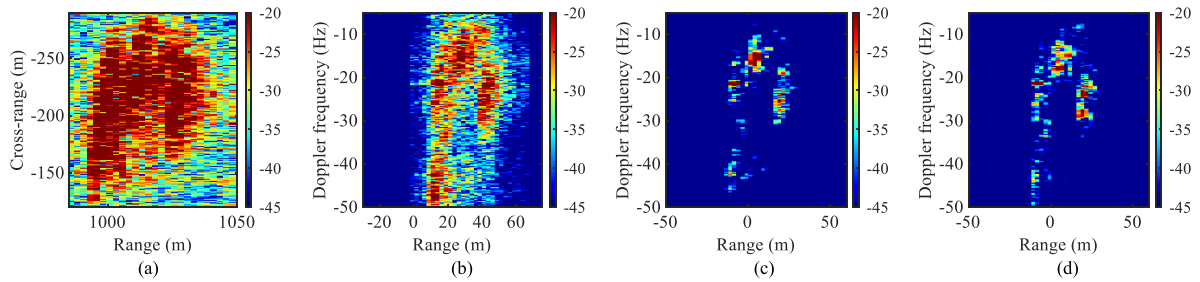

Fig. 19. Imaging results of the 3rd ship target. (a) SAR image. (b) ISAR image with RD approach. (c) and (d) Refocused instantaneous ISAR images via the RID approach.
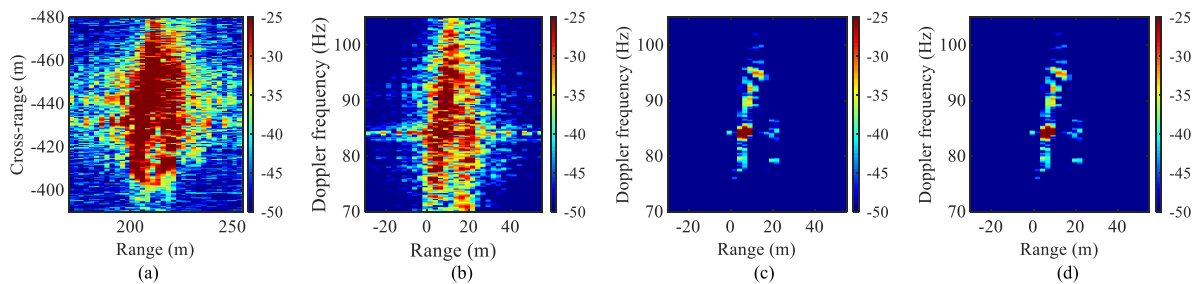

Fig. 20. Imaging results of the 4th ship target. (a) SAR image. (b) ISAR image with RD approach. (c) and (d) Refocused instantaneous ISAR images via the RID approach.
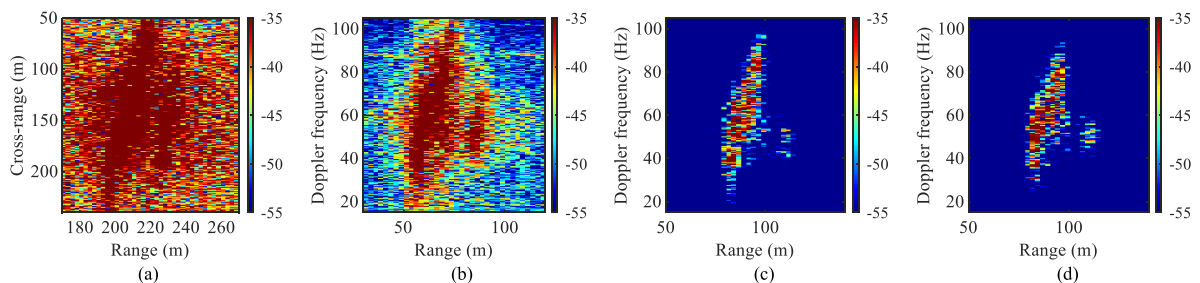

Fig. 21. Imaging results of the 5th ship target. (a) SAR image. (b) ISAR image with RD approach. (c) and (d) Refocused instantaneous ISAR images via the RID approach.
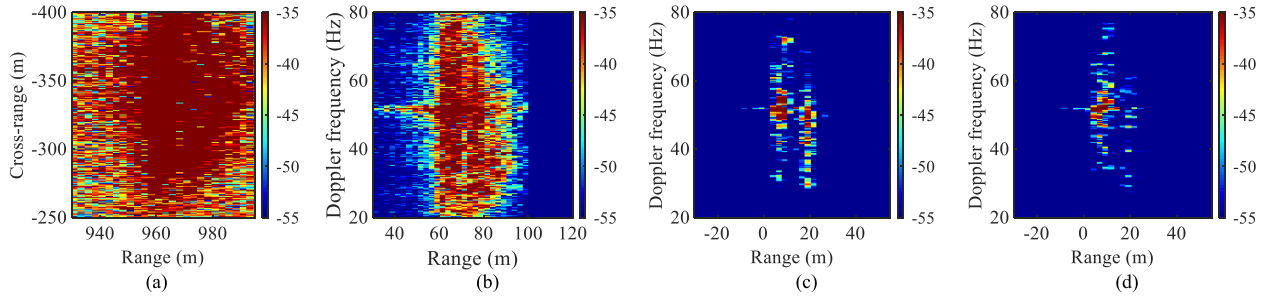
Fig. 22.   Imaging results of the 6th ship target. (a) SAR image. (b) ISAR image with RD approach. (c) and (d) Refocused instantaneous ISAR images via the RID approach.
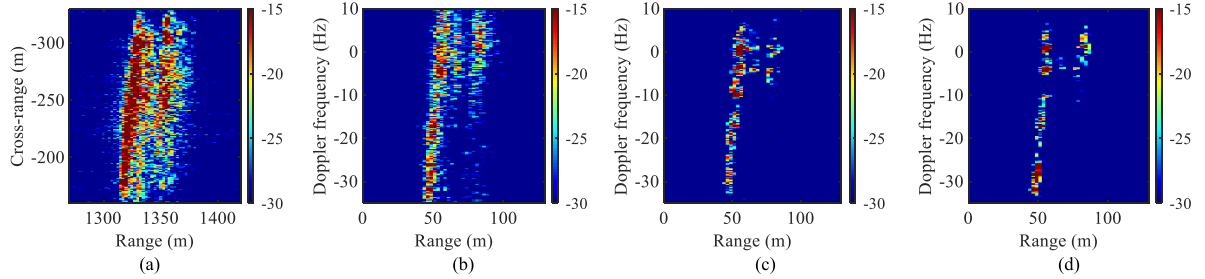

Fig. 23.   Imaging results of the 7th ship target. (a) SAR image. (b) ISAR image with RD approach. (c) and (d) Refocused instantaneous ISAR images via the RID approach.
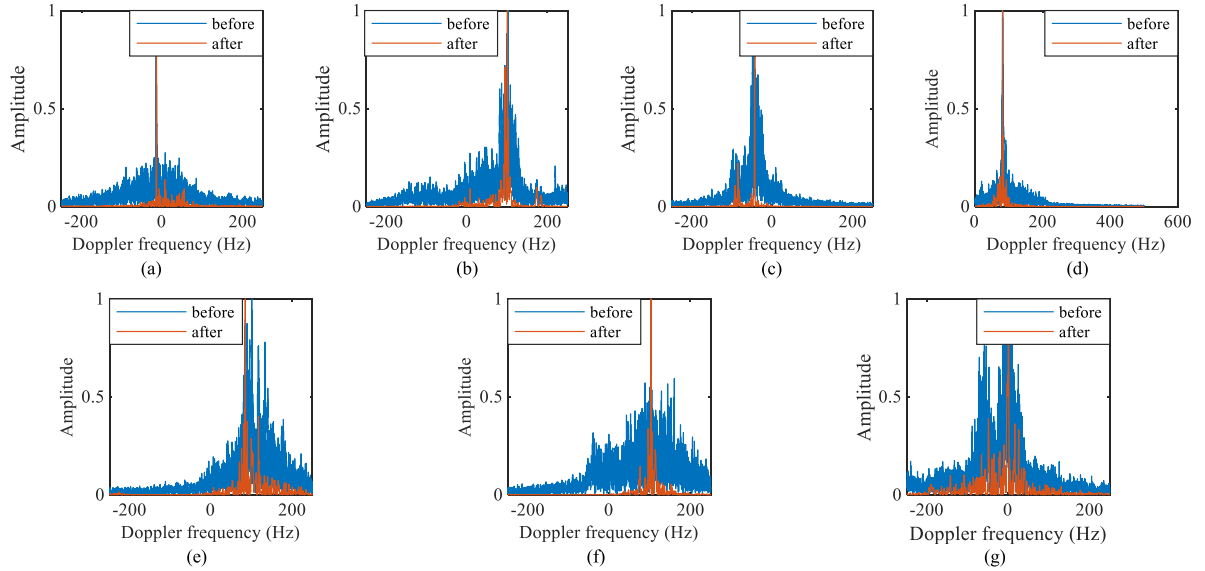

Fig. 24.   Azimuth profile in one range bin before and after RID imaging. (a)–(g) are the azimuth profile of the first to seventh ship target before and after RID imaging.

ship targets before and after RID imaging are shown in Fig. 24. From Fig. 24(a)–(g), it is apparent that the azimuth profiles are well focused after ISAR refocusing.

VI. CONCLUSION

Combining SAR algorithm with ISAR technique, the focused and clear images of ship targets on the sea surface can be obtained. Whereas, the manual image segmentation and refocusing consume large manpower that limits applications on

multiple actual situations. In this article, for improving the imaging efficiency and easing the manual labor, an automatic hybrid SAR/ISAR imaging algorithm is proposed including the automatic image segmentation, inverse mapping, and ISAR refocusing. First, the SAR processing method we adopt is introduced and derived. Then, the residual phase of the processed signal is deduced in detail for illustrating the necessity of utilizing the ISAR refocusing technique. Afterward, an automatic ISAR refocusing algorithm is proposed, which contains the automatic image segmentation, inverse mapping, and ISAR imaging. The

clustering algorithm can attain the 2-D scopes of ship targets and achieve the automatic image segmentation. Additionally, the equivalent data of each target can be obtained via inverse mapping. Afterward, the identical movement of all scatterers can be eliminated via the motion compensation in ISAR processing, while the diverse movements via the RID technique. Finally, the clear and refocused images of ship targets can be generated. Compared with the existed hybrid SAR/ISAR algorithm, the proposed algorithm is automatic, labor-saving, and considering the complicated motions of ship targets. At last, the imaging results of simulated and real measured data validate the availability of the presented algorithm.

REFERENCES

[1] X. Jiang, G. Li, Y. Liu, X. Zhang, and Y. He, "Change detection in heterogeneous optical and SAR remote sensing images via deep homogeneous feature fusion," *IEEE J. Sel. Topics Appl. Earth Observ. Remote Sens.*, vol. 13, pp. 1551–1566, Apr. 2020.

[2] J. F. Shi, H. Y. Jin, and X. H. Li, "A novel multi-feature joint learning method for fast polarimetric SAR terrain classification," *IEEE Access*, vol. 8, pp. 30491–30503, 2020.

[3] D. M. Song *et al.*, "A novel marine oil spillage identification scheme based on convolution neural network feature extraction from fully polarimetric SAR image," *IEEE Access*, vol. 8, pp. 59801–59820, 2020.

[4] M. Martorella *et al.*, "ISAR based technique for refocusing non-cooperative targets in SAR images," *IET Radar, Sonar Navig.*, vol. 6, no. 5, pp. 332–340, Jun. 2012.

[5] Y. C. Jiang and H. Y. Wang, "Hybrid SAR/ISAR imaging of ship targets based on parameter estimation," *Remote Sens. Lett.*, vol. 8, no. 7, pp. 657–666, 2017.

[6] M. Martorella, D. Pastina, F. Berizzi, and P. Lombardo, "Spaceborne radar imaging of maritime moving targets with the Cosmo-skymed SAR system," *IEEE J. Sel. Topics Appl. Earth Observ. Remote Sens.*, vol. 7, no. 7, pp. 2797–2810, Jul. 2014.

[7] V. C. Chen and B. Liu, "Hybrid SAR/ISAR for distributed ISAR imaging of moving targets," in *Proc. IEEE Radar Conf.*, May 2015, pp. 10–15.

[8] Z. S. Yan *et al.*, "An ISAR approach for refocusing the maritime moving targets with the GF-3 SAR satellite," in *Proc. 6th Asia-Pacific Conf. Synthetic Aperture Radar*, 2019, pp. 1–5.

[9] H. D. Sun, L. Zhou, J. Z. Ma, and X. Y. Liu, "The hybrid SAR-ISAR imaging algorithm applied to SAR moving target imaging," in *Proc. 9th Int. Conf. Fuzzy Syst. Knowl. Discov.*, 2012, pp. 1985–1988.

[10] C. Yeh, J. Yin, and J. Yang, "Hybrid SAR/ISAR imaging of ground moving target with along-track airborne bi-static SAR," in *Proc. Int. Conf. Electron., Commun. Control*, 2011, pp. 4340–4343.

[11] R. Pelich *et al.*, "Ship refocusing and velocity estimation on SAR image using the fractional fourier transform," *IEEE Trans. Geosci. Remote Sens.*, vol. 54, no. 3, pp. 1670–1684, Mar. 2016.

[12] J. K. Jao, "Theory of synthetic aperture radar imaging of a moving target," *IEEE Trans. Geosci. Remote Sens*, vol. 39, no. 9, pp. 1984–1992, Sep. 2001.

[13] Z. Zhou, Z. Ding, T. Zhang, and Y. Wang, "High-Squint SAR imaging for noncooperative moving ship target based on high velocity motion platform," in *Proc. China Int. SAR Symp.*, 2018, pp. 1–5.

[14] J. Yang and Y. Zhang, "Squint SAR ground moving target imaging and motion parameters estimation with keystone transform," in *Proc. Asia-Pac. Microw. Conf.*, 2018, pp. 827–829.

[15] D. Gu, H. Yue, B. Lu, and X. Xu, "Velocity estimation for moving target refocusing in the long-time coherent integration SAR imaging," in *Proc. China Int. SAR Symp.*, 2018, pp. 1–4.

[16] S. Zhou, Z. Xu, and F. Liu, "Method for determining the optimal number of clusters based on agglomerative hierarchical clustering," *IEEE Trans. Neural Netw. Learn. Syst.*, vol. 28, no. 12, pp. 3007–3017, Dec. 2017.

[17] I. Cattinelli, G. Valentini, E. Paulesu, and N. A. Borghese, "A novel approach to the problem of non-uniqueness of the solution in hierarchical clustering," *IEEE Trans. Neural Netw. Learn. Syst.*, vol. 24, no. 7, pp. 1166–1173, Jul. 2013.

[18] C.-R. Lin and M.-S. Chen, "Combining partitional and hierarchical algorithms for robust and efficient data clustering with cohesion self-merging," *IEEE Trans. Knowl. Data Eng.*, vol. 17, no. 2, pp. 145–159, Feb. 2005.

[19] D. Lee, S. Baek, and K. Sung, "Modified K-means algorithm for vector quantizer design," *IEEE Signal Process. Lett.*, vol. 4, no. 1, pp. 2–4, Jan. 1997.

[20] J. K. Parker and L. O. Hall, "Accelerating Fuzzy-C means using an estimated subsample size," *IEEE Trans. Fuzzy Syst.*, vol. 22, no. 5, pp. 1229–1244, Oct. 2014.

[21] Y. Li, T. Su, J. Zheng, and X. He, "ISAR imaging of targets with complex motions based on modified Lv's distribution for cubic phase signal," *IEEE J. Sel. Topics Appl. Earth Observ. Remote Sens.*, vol. 8, no. 10, pp. 4775–4784, Oct. 2015.

[22] J. Zheng, H. Liu, G. Liao, T. Su, Z. Liu, and Q. H. Liu, "ISAR imaging of nonuniformly rotating targets based on generalized decoupling technique," *IEEE J. Sel. Topics Appl. Earth Observ. Remote Sens.*, vol. 9, no. 1, pp. 520–532, Jan. 2016.

[23] J. Zheng, T. Su, G. Liao, H. Liu, Z. Liu, and Q. H. Liu, "ISAR imaging for fluctuating ships based on a fast bilinear parameter estimation algorithm," *IEEE J. Sel. Topics Appl. Earth Observ. Remote Sens.*, vol. 8, no. 8, pp. 3954–3966, Aug. 2015.

[24] W. Rao, G. Li, X. Wang, and X. Xia, "Adaptive sparse recovery by parametric weighted L_1 minimization for ISAR imaging of uniformly rotating targets," *IEEE J. Sel. Topics Appl. Earth Observ. Remote Sens.*, vol. 6, no. 2, pp. 942–952, Apr. 2013.

[25] J. Wang, L. Zhang, L. Du, D. Yang, and B. Chen, "Noise-Robust motion compensation for aerial maneuvering target ISAR imaging by parametric minimum entropy optimization," *IEEE Trans. Geosci. Remote Sens*, vol. 57, no. 7, pp. 4202–4217, Jul. 2019.

[26] Z. G. Ding *et al.*, "A ship ISAR imaging algorithm based on generalized radon-fourier transform with low SNR," *IEEE Trans. Geosci. Remote Sens*, vol. 57, no. 9, pp. 6385–6396, Sep. 2019.

[27] F. Berizzi, E. D. Mese, M. Diani, and M. Martorella, "High-resolution ISAR imaging of maneuvering targets by means of the range instantaneous doppler technique: Modeling and performance analysis," *IEEE Trans. Image Process.*, vol. 10, no. 12, pp. 1880–1890, Dec. 2001.

[28] G. Li and P. K. Varshney, "Micro-Doppler parameter estimation via parametric sparse representation and pruned orthogonal matching pursuit," *IEEE J. Sel. Topics Appl. Earth Observ. Remote Sens.*, vol. 7, no. 12, pp. 4937–4948, Dec. 2014.

[29] V. C. Chen and S. Qian, "Joint time-frequency transform for radar range-Doppler imaging," *IEEE Trans. Aerosp. Electron. Syst.*, vol. 34, no. 2, pp. 486–499, Apr. 1998.

[30] V. C. Chen and H. Ling, *Time-Frequency Transforms for Radar Imaging and Signal Analysis*. Norwood, MA, USA: Artech House, 2002.

[31] Y. Wang, R. Cao, and X. Huang, "ISAR imaging of maneuvering target based on the estimation of time varying amplitude with Gaussian window," *IEEE Sens. J.*, vol. 19, no. 23, pp. 11180–11191, Dec. 2019.

[32] X. Bai, R. Tao, Z. Wang, and Y. Wang, "ISAR imaging of a ship target based on parameter estimation of multicomponent quadratic frequency modulated signals," *IEEE Trans. Geosci. Remote Sens.*, vol. 52, no. 2, pp. 1418–1429, Feb. 2014.

[33] M. Bao, M. D. Xing, Y. C. Li, and Y. Wang, "Two-dimensional spectrum for MEO SAR processing using a modified advanced hyperbolic range equation," *Electron. Lett.*, vol. 47, no. 18, pp. 1043–1045, Sep. 2011.

[34] N. Otsu, "A threshold selection method from gray-level histograms." *IEEE Trans. Syst., Man, Cybern.*, vol. 9, no. 1, pp. 62–66, Jan. 1979.

[35] D. Zhu, L. Wang, Y. Yu, Q. Tao, and Z. Zhu, "Robust ISAR range alignment via minimizing the entropy of the average range profile," *IEEE Geosci. Remote Sens. Lett.*, vol. 6, no. 2, pp. 204–208, Apr. 2009.

[36] X. H. Qiu, Y. Zhao, and S. Udpa, "Phase compensation for ISAR imaging combined with entropy principle," in *Proc. IEEE Antennas Propag. Soc. Int. Symp. Dig. USNC/CNC/URSI North Amer. Radio Sci. Meeting*, 2003, pp. 195–198.

[37] D. Margaret. "Core topics," in *Data Mining Introductory and Advanced Topics*. Britain, NJ, USA: Pearson Education, 2006.
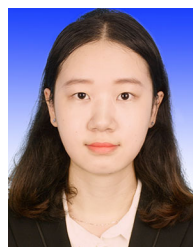
Rui Cao was born in 1996. She received the B.S. degree in electronic information engineering and the M.S. degree in information and communication engineering from the Harbin Institute of Technology, Weihai, China, in 2018 and 2020, respectively. She is currently working toward the Ph.D. degree in information and communication engineering from the HIT, Harbin, China.

Her current research interests include the field of ISAR imaging and radar signal processing.

Yong Wang was born in 1979. He received the B.S. and M.S. degrees from the Harbin Institute of Technology (HIT), Harbin, China, in 2002 and 2004, respectively, both in electronic engineering, and the Ph.D. degree in information and communication engineering from HIT in 2008.

He is currently a Professor with the Institute of Electronic Engineering Technology, HIT. He has authored or authored more than 130 papers, most of them appeared in the journals of the IEEE TRANSACTIONS ON GEOSCIENCE AND REMOTE SENSING, *IET Signal Processing, Signal Processing,* etc. His main research interests include time.]frequency analysis of nonstationary signal, radar signal processing, and their application in synthetic aperture radar (SAR) imaging.

Dr. was the recipient of the Program for New Century Excellent Talents in the University of Ministry of Education of China in 2012 and the Excellent Doctor's Degree nomination Award in China in 2010.

Xiaofei Lu was born in 1981. He received the B.S. and M.S. degrees from the Harbin Institute of Technology (HIT), Harbin, China, in 2002 and 2004, respectively, both in electronic engineering, and the Ph.D. degree in control theory and control engineering from Tsinghua University, Beijing, China, in 2012.

He is currently an Engineer with JiuQuan Satellite Launch Center. His main research interests include target recognition, radar signal processing, and their practical application. He has authored or coauthored more than 20 papers.

Bin Zhao was born in 1972. He received the B.S. and M.S. degrees from the Harbin Institute of Technology (HIT), Harbin, China, in 1988 and 1998, respectively, both in electronic engineering, and the Ph.D. degree in information and communication engineering from HIT in 2008.

He is currently a Professor with the Institute of Electronic Engineering Technology, HIT. His main research interests include radar system control and synthetic aperture radar (SAR) imaging.